Fermi National Accelerator Laboratory

FERMILAB-Conf-81/80-EXP
7420.616

RECENT RESULTS ON TOTAL NEUTRINO AND ANTINEUTRINO CROSS SECTIONS BY THE CFRR COLLABORATION*

B. C. Barish, R. E. Blair, Y. K. Chu, B. N. Jin,
D. B. MacFarlane, R. L. Messner, J. R. Lee, J. Ludwig,
D. B. Novikoff, and M. V. Purohit
California Institute of Technology, Pasadena, California 91125

and

F. J. Sciulli and M. H. Shaevitz
Columbia University, New York, New York 10027

and

F. J. Bartlett, D. A. Edwards, H. T. Edwards, H. E. Fisk,
Y. Fukushima, Q. A. Kerns, T. Kondo, P. A. Rapidis,
S. L. Segler, R. J. Stefanski, D. E. Theriot, and
D. D. Yovanovitch
Fermi National Accelerator Laboratory, Batavia, Illinois 60510

and

A. Bodek, R. N. Coleman, and W. L. Marsh
University of Rochester, Rochester, New York 14627

and

O. D. Fackler and K. A. Jenkins
Rockefeller University, New York, New York 10021

December 1981

---

*Talk presented by P. A. Rapidis at the Summer Institute on Particle Physics, Stanford Linear Accelerator Center, Stanford, California, July 27-August 7, 1981.

RECENT RESULTS ON TOTAL NEUTRINO AND ANTINEUTRINO CROSS SECTIONS BY THE CFRR COLLABORATION

B.C. Barish, R.E. Blair, Y.K. Chu, B.N. Jin[1], D.B. MacFarlane,
R.L. Messner[2], J.R. Lee[3], J. Ludwig[4], D.B. Novikoff[5], M.V. Purohit
California Institute of Technology, Pasadena, California 91125

F.J. Sciulli, M.H. Shaevitz
Columbia University, New York, New York 10027

F.J. Bartlett, D.A. Edwards, H.T. Edwards, H.E. Fisk, Y. Fukushima[6],
Q.A. Kerns, T. Kondo[6], P.A. Rapidis, S.L. Segler, R.J. Stefanski,
D.E. Theriot, D.D. Yovanovitch
Fermi National Accelerator Laboratory, Batavia, Illinois 60510

A. Bodek, R.N. Coleman[1], W.L. Marsh[1]
University of Rochester, Rochester, New York 14627

O.D. Fackler, K.A. Jenkins
Rockefeller University, New York, New York 10021

Talk presented by P.A. Rapidis at the Summer Institute on Particle Physics, Stanford Linear Accelerator Center, Stanford, California, July 27 - August 7, 1981.

ABSTRACT

We present results on normalized cross sections for charged current neutrino and antineutrino-nucleon scattering. The cross sections can be parametrized as a linearly rising function of the incident neutrino energy, with $\sigma_\nu/E = 0.720\pm0.030\times10^{-38}$ and $\sigma_{\bar\nu}/E = 0.360\pm0.023\times10^{-38}$ cm^2/GeV. These results are ~15% higher than previous measurements. Preliminary structure functions at low Q^2 are also presented.

Present addresses:

1. Fermi National Accelerator Laboratory, Batavia, Illinois 60510
2. Stanford Linear Accelerator Center, Stanford, California 94305
3. Sandia Laboratories, Albuquerque, New Mexico 87185
4. Albert Ludwigs University, Freiburg, West Germany
5. Hughes Aircraft Company, El Segundo, California 90245
6. National Laboratory for High Energy Physics, Tsukuba-gun, Ibaraki-ken 305, Japan

I. Motivation

Lepton-nucleon scattering has proven to be one of the most successful techniques used for the study of the nucleon structure. Much of today's acceptance of the constituent quark model can be traced to the verification of the model's predictions by lepton-nucleon scattering. Such predictions in the case of neutrino-nucleon interactions include the scaling of structure functions, which, in turn, implies cross sections that rise linearly with the energy of the incident neutrino. A more detailed analysis that incorporates the effects of quark binding and gluon exchange is not expected to significantly modify this linear energy dependence. In addition, the slope of the total cross section, i.e. σ_ν/E_ν, is related directly to the integrals of the structure functions and, in this sense, determines the overall normalization of the measured structure functions.

Many of the tests of the quark model are sensitive to this normalization. Such tests include:

1) The comparison of $F_2(x)$ determined from neutrino-nucleon and electron/muon-nucleon scattering. We should have, aside from effects due to the strange and charmed sea:

$$F_2^{\nu N}(x) = \frac{18}{5} F_2^{eN}(x),$$

where the 5/18 factor is due to the mean-square charge of the nucleon's quarks.

2) The fraction of the nucleon's momentum carried by quarks.

3) The determination of the number of valence quarks from the Gross-Llewelyn-Smith sum rule, i.e.:

$$\int \frac{x\,F_3(x)}{x}\,dx = 3,$$

where 3 is the number of valence quarks.

Furthermore, if σ_ν/E_ν is not a constant this may be an indication of propagator effects or of exotic behaviour (e.g. neutrino oscillations).

Past measurements of cross-sections and structure functions show agreement with the predictions of the quark model at the 20% level. The need for a more precise measurement of these quantities has led us to perform an accurate neutrino-nucleon scattering experiment at the Fermi National Accelerator Laboratory (Experiment 616). We report here measurements of neutrino and anti-neutrino charged current total cross sections and preliminary measurements of structure functions from our experiment. Our results for the total cross sections are approximately 15% higher than previously reported measurements. This difference could affect comparisons to quark model predictions[1].

II The Dichromatic Beam

The total charged current cross section in a certain neutrino energy range is given by:

$$\sigma = C\,\frac{N_{ev}}{F_\nu\,N_n} \quad ,$$

where N_{ev} is the total number of charged current events occurring in our detector, F_ν is the total number of neutrinos incident on our detector, and N_n is the total number of nucleons in our detector. C is a constant that incorporates small corrections (<6%) to the number of events due to unsampled kinematic regions. It is obvious that an accurate measurement of the cross section neccessitates an accurate determination of the integrated neutrino flux. A description of our flux measuring technique is in order.

The neutrinos used in our experiment are produced in the decay of (roughly) monochromatic pions and kaons. The overall arrangement is shown in Fig. 1. 400 GeV/c protons from Fermilab's proton synchrotron impinge on a 12" long BeO target located at the beginning of the N-30 dichromatic train[2]. Charged secondaries (pions, kaons and protons) produced in the forward direction ($\theta < 1.6$ mrad) of a selected sign and momentum ($\Delta p/p = 9.4\%$) are transported through the train (a specially designed point-to-parallel beam channel) and are allowed to travel through a 340m long evacuated decay path. It is in this part of the beam line that some of the pions and kaons decay into neutrinos and muons. The surviving secondary hadrons, as well as the decay muons, are stopped by a beam dump followed by a 910m long earth shield. The neutrinos travel through the shield, with negligible attenuation of their flux, and some of them interact with our detector located in Lab E at the end of the earth shield.

The neutrino flux, due to the rather elusive nature of the neutrino, is not a directly measureable quantity. It is essentially derived from the following equation:

$$F_{\nu} = N_{\mathrm{beam}} \times f_{\pi \text{ or } K} \times D \times A ,$$

where N_{beam} is the number of charged particles in the secondary beam, and includes the number of secondary pions, kaons, protons and electrons, $f_{\pi \text{ or } K}$ is the fraction of pions or kaons in the secondary beam, D is the probability that π's or K's will decay in their decay path, and A is a factor that corrects for the finite angular acceptance of our apparatus. It is one of the major advantages of the dichromatic beam that the monochromatic nature of the secondaries and its small angular divergence make an accurate measurement of all of these factors

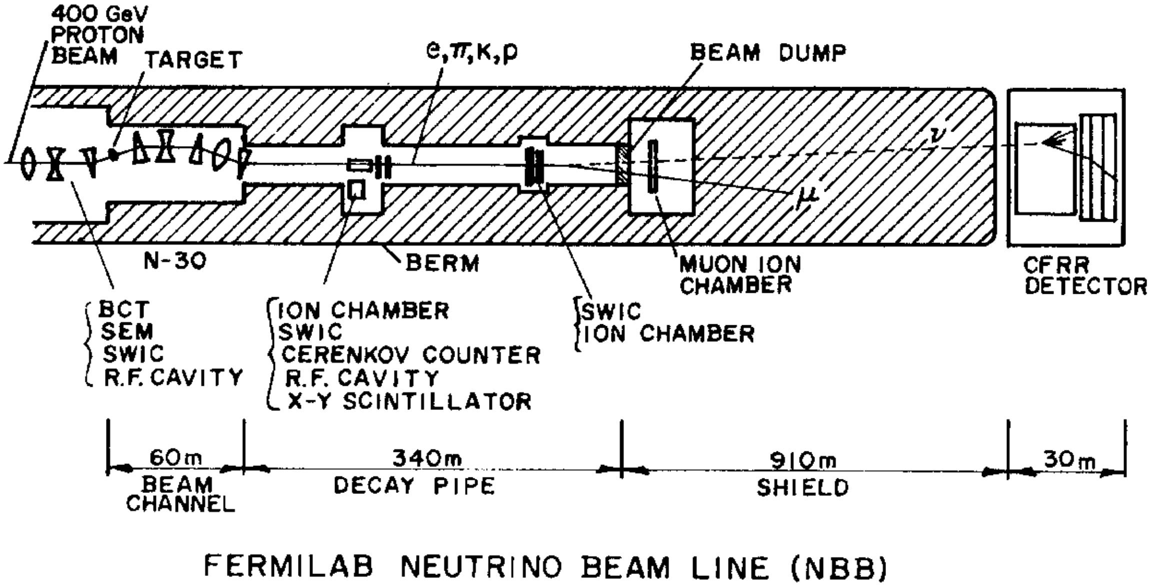

<u>Fig. 1:</u> Layout of Fermilab's Narrow Band Neutrino Beam line. Note that its dimensions are not properly scaled and that the transverse dimension of the beam has been expanded relative to the longitudinal dimension by approximately a factor of 100. Abbreviations occurring in the figure are BCT: Beam Current Transformer, SEM: Secondary Emission Monitor, SWIC: Segmented Wire Ion Chamber.

possible. We shall now embark on a detailed description of how each one of these factors was determined.

A combination of detectors was used to measure the flux of secondaries N_{beam}. Our primary devices were ion chambers placed at two locations along the decay pipe (see Figs. 1 and 2). At each of these locations we had three independent ion chamber gaps that allowed for cross checks to be made thoughout the running period. The collected charge in each gap was converted to pulse trains by high-speed, small current digitizers[3], which were calibrated continously by injecting into them a known amount of charge between machine pulses. The long term stability and the linearity of these ion chambers are illustrated by Figs. 3 and 4. Run-to-run fluctuations in their response were on the average ~2% for neutrino running (positive secondaries) and ~5% for antineutrino running. The linearity was better than 1%.

The absolute calibration of the ion chambers was measured in four different ways:

a) <u>By foil activation:</u> 200 GeV/c primary protons were transported through the train (with the target removed) and the decay pipe. The response of the ion chamber as well as the amount of Na^{24} produced in a thin Cu foil placed in front of the ion chamber were measured. We obtained for our ion chamber a response of 3.53 ± 0.10 pC/10^6 particles based on the cross-section for the production for Na^{24} (3.83 ± 0.07mb) as measured in a CERN experiment[4] (that used a beam current transformer).

b) <u>By using the beam current transformer and foil activation:</u> In this case a beam current transformer was used to measure the 200 GeV/c primary proton flux and a set of Cu foils (one before and one after the N-30 dichromatic train) were used to measure the fraction of protons transmitted through the train. We found that the ion chamber response was 3.58 ± 0.17 pC/10^6 particles. As by-products the train transmission was measured to be $92.5 \pm 5\%$ (design calculation: 95.5%) and the Na^{24}

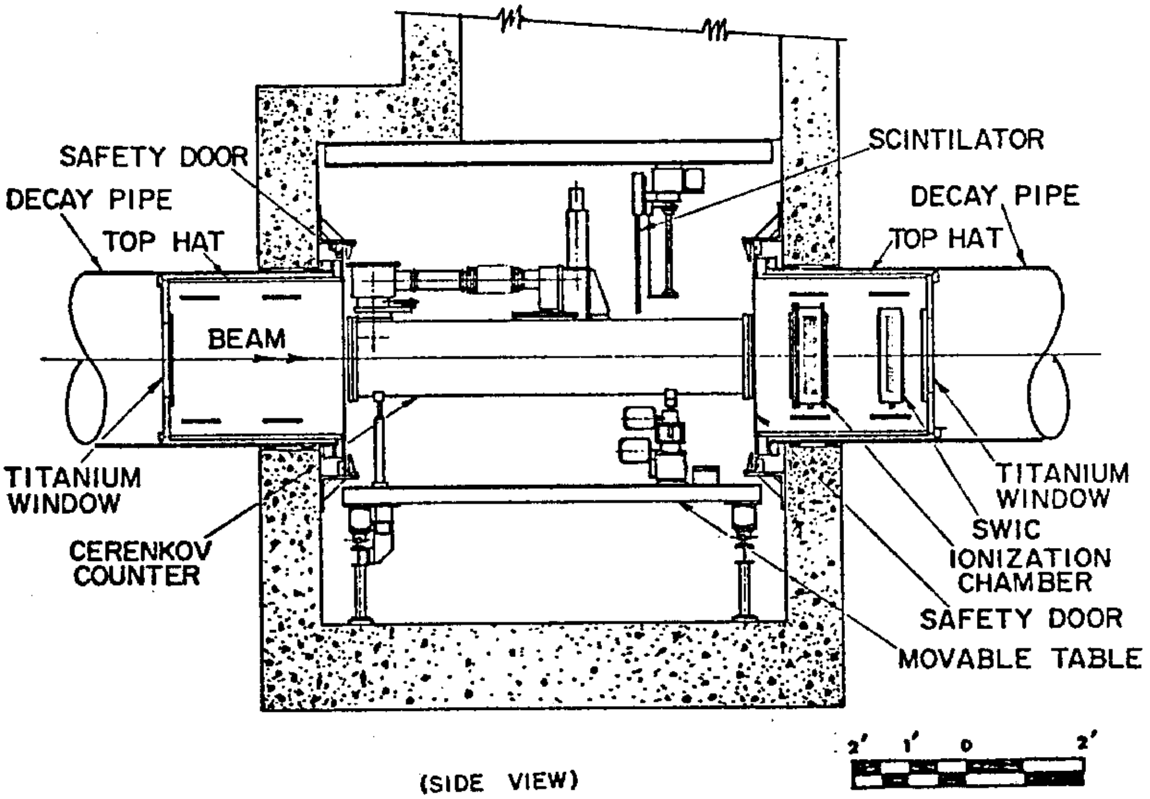

(SIDE VIEW)

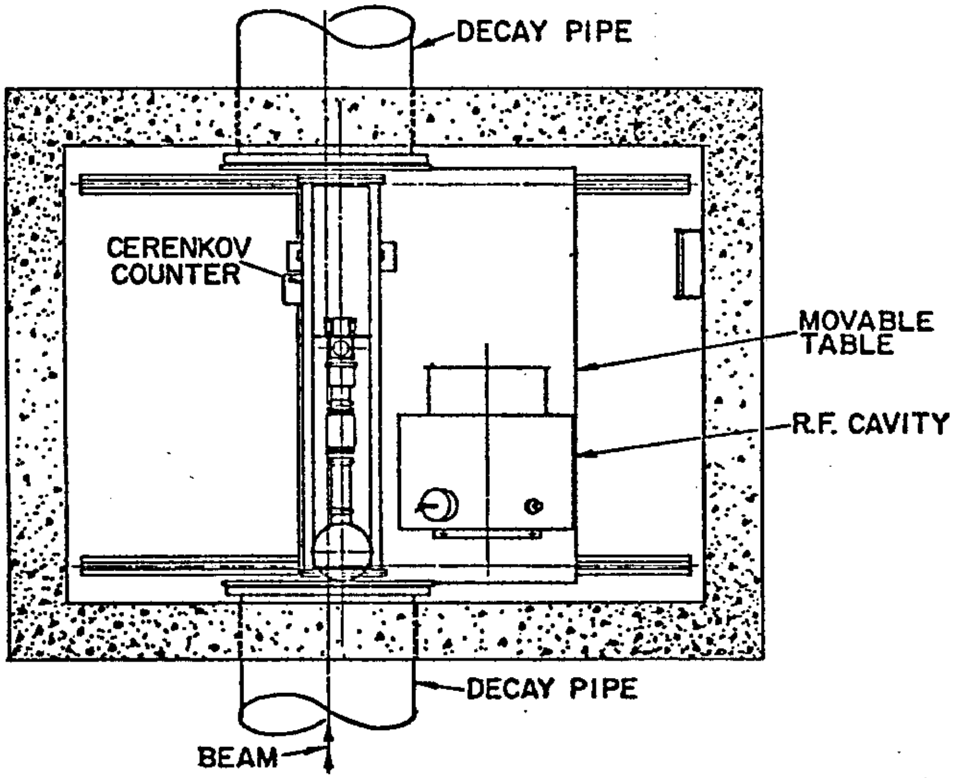

(PLAN VIEW)

Fig. 2: Layout of monitoring equipment in the first (upstream) monitoring station. The Cerenkov counter and the R.F. cavity were mounted on a movable table; thus we could position either the R.F. caviy or the Cerenkov counter in the beam.

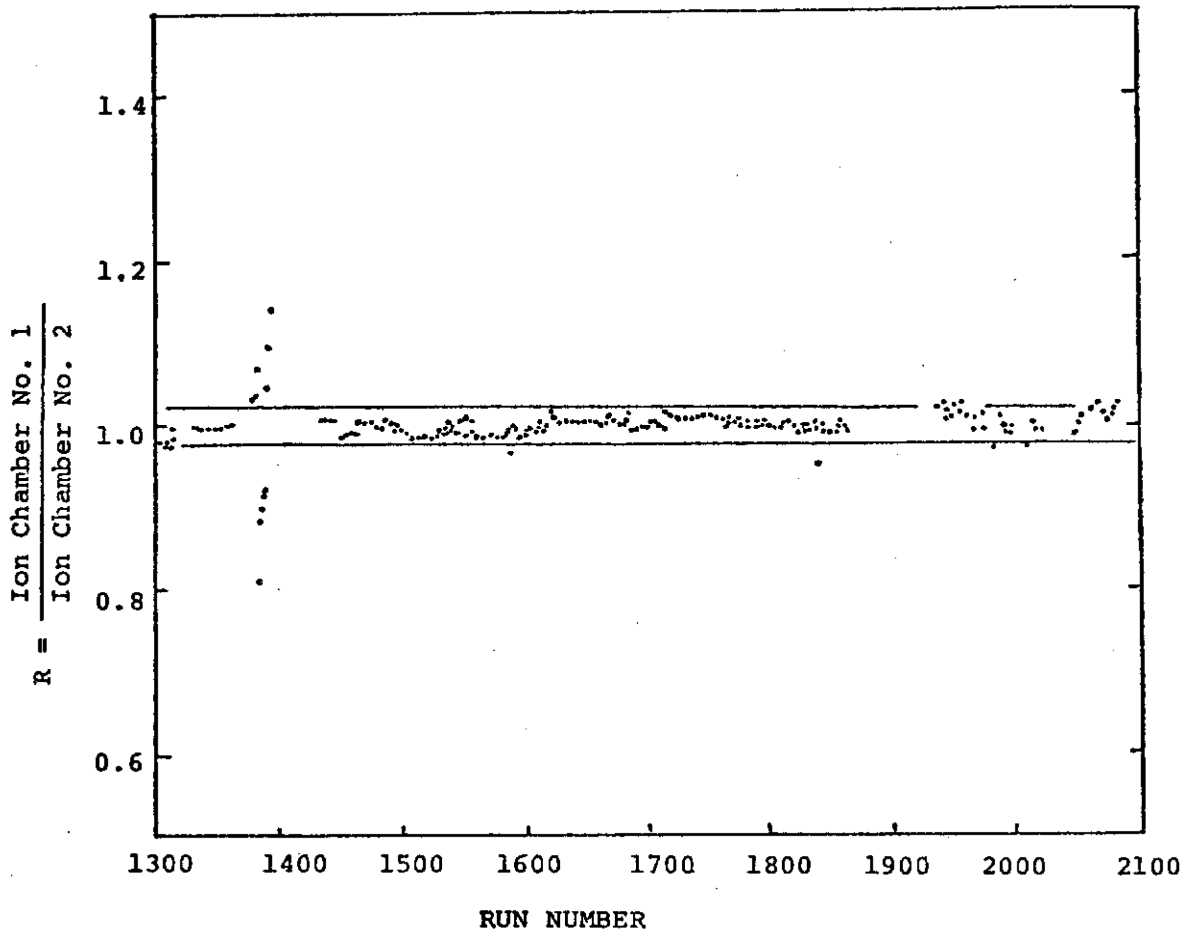

Fig. 3: Ratio of the response of ion chamber No. 1 (located in the upstream monitoring station) to the response of ion chamber No. 2 (located in the downstream monitoring station) versus run number. These runs span a time period of a little more than 100 days. The abnormal behaviour of this ratio near run 1380 is due to a variety of tests that were being performed on chamber 1 at the time and is not indicative of normal operation. The two horizontal lines indicate the ±2% band. It should be noted that a) the two chambers are separated by 140m and that they have independent gas circulation systems and electronics, b) during this period the momentum of the dichromatic train was changed numerous times, but it was set to transport positive secondaries for more than 80% of the runs shown.

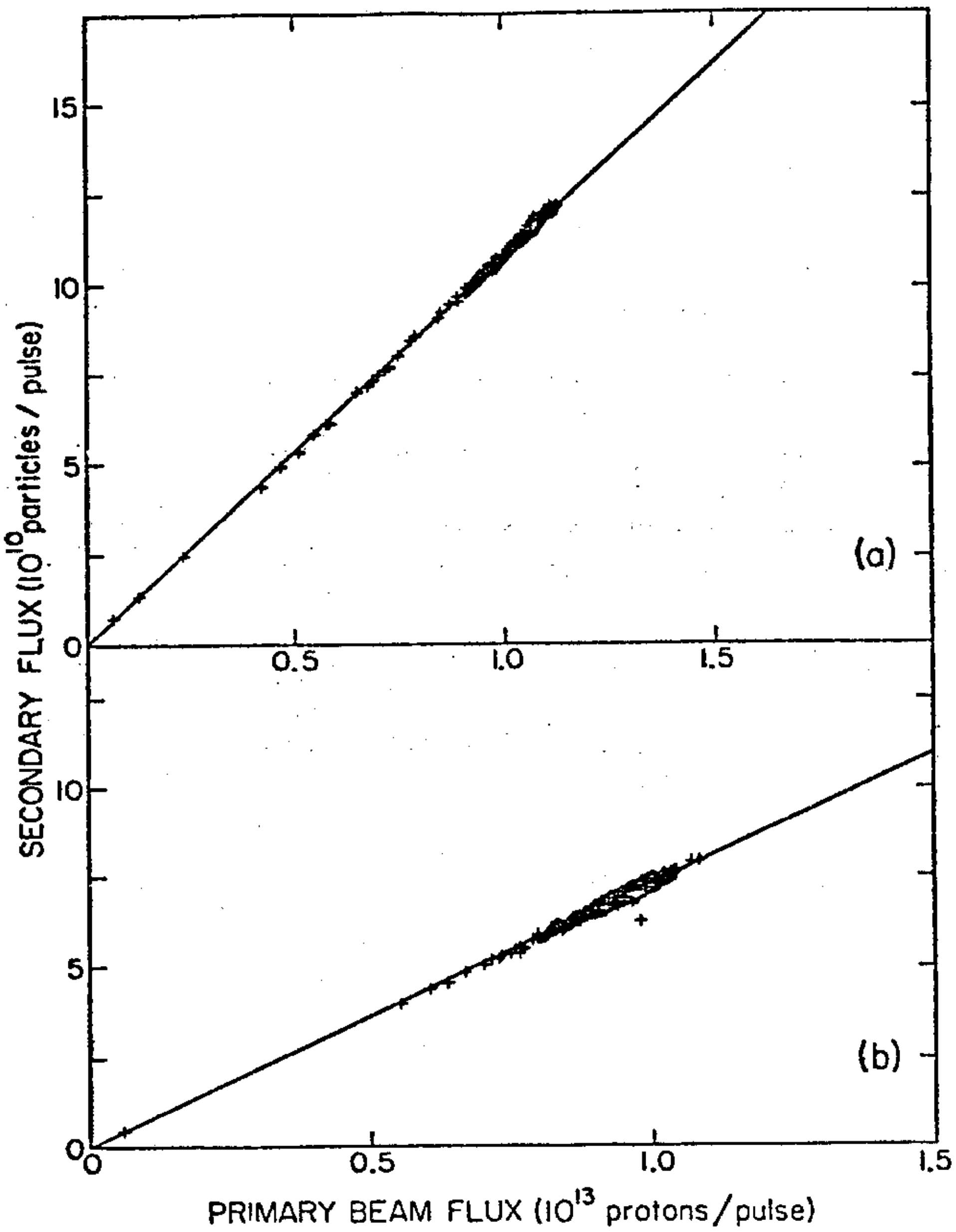

Fig. 4: Secondary flux for a single machine pulse as determined by the upstream ionization chamber versus the primary beam intensity as measured by (a) the secondary emission monitor (SEM) and (b) the beam current transformer. The dichromatic train was set to transport positive secondaries of 250 GeV/c momentum for the data in (a) and of 200 GeV/c for the data in (b).

production cross section in Cu was determined to be 3.91± 0.20 mb.

c) By using an R.F. beam intensity monitor: For most of the data taking period a resonant R.F. cavity was placed in front of the ion chamber (see Figs. 2 and 5). This device exploits the short time-scale structure of the extracted proton beam at Fermilab (which can be modeled as buckets having a shape similar to $\cos^2(\ t/5\text{ns})$ repeating every 18.83 ns) to produce an output proportional to the intensity of the beam. In addition, the response of this device can be absolutely calibrated using simple R.F. measurements of its characteristics.

It should be noted in passing that the R.F. cavity provided an additional cross-check on the linearity and stability of our ion chambers (see Fig. 6).

Using the R.F. cavity we obtained an ion chamber response of 3.58 ± 0.17 pC/10^6 particles for 200 GeV/c primary protons and an average response of 3.46 ± 0.17 (point-to-point variation) ± 0.20 (systematic) pC/10^6 particles for the secondaries used throughout our running (±120, ±140, ±168, ±200, ±250 GeV/c particles). During the course of this study we found that the ion chamber response versus the R.F. cavity response showed a 6% variation with beam energy and beam polarity. After considerable study of the R.F. cavity in the extracted proton beam we eliminated as probable causes any changes in the R.F. cavity response due to material in the beam (such as δ rays produced in the air gap of the cavity, gaseous plasma shielding the beam, etc.). We also established that the R.F. cavity response and the response of the beam current transformer monitoring the intensity of the extracted proton beam agreed with each other at the 2-3% level. In order to understand this variation we resorted to a fourth technique:

d) By counting particles: In this method, we calibrated the ion chamber directly with a low intensity secondary beam and single particle counting. Measurements were made at four different momenta with

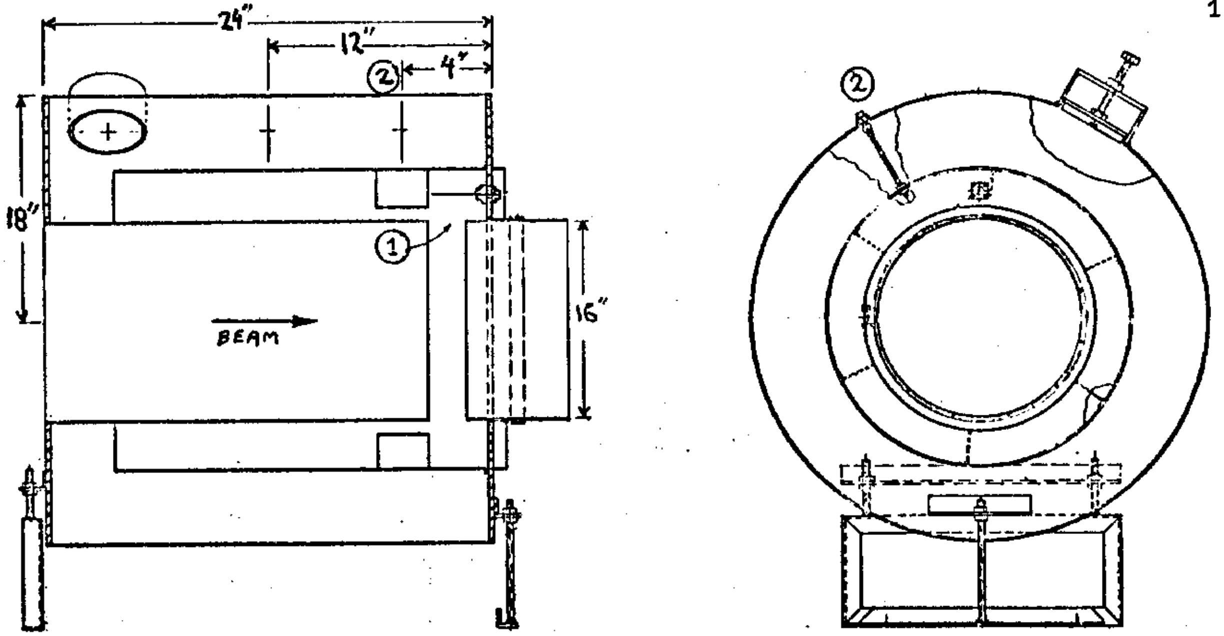

Fig. 5: R.F. Cavity Beam intensity monitor. The cavity is a folded 20 ohm coaxial transmission line. One end is shorted to form a quarter wave resonator tuned to 53.104 MHz with a loaded Q~230. (1) is the gap excited by the R.F. structure of the beam and (2) is a magnetic loop tap.

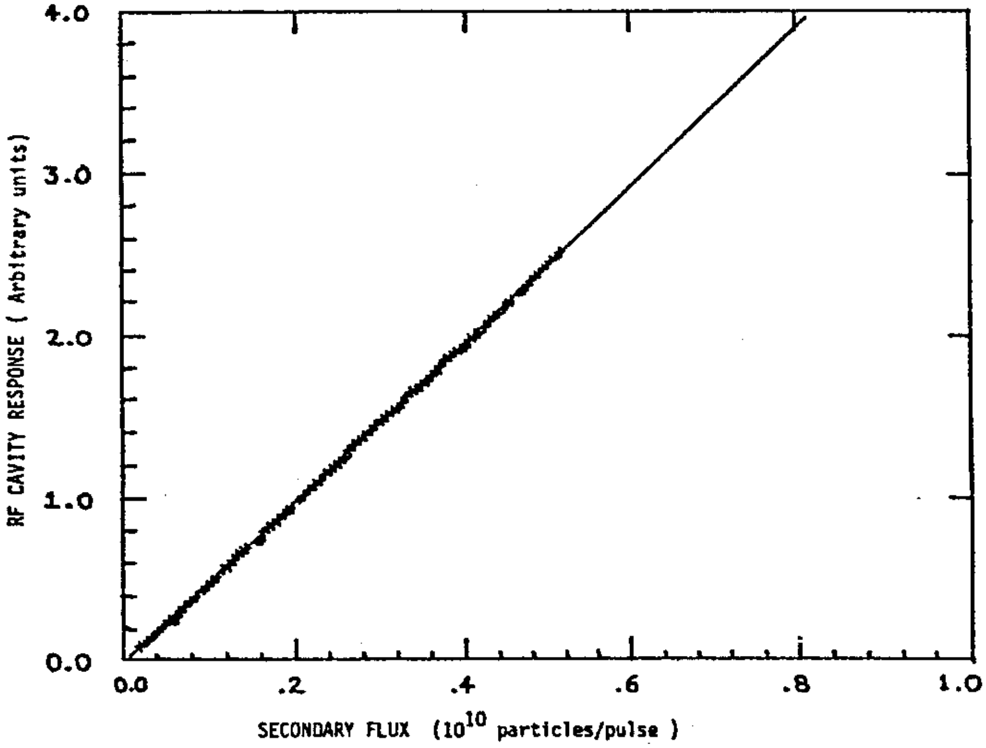

Fig. 6: Response of the R.F. Cavity versus the secondary flux measured by the ion chamber for negative 120 GeV/c secondaries. It should be noted that the two techniques depend on two completely different physical processes, i.e. excitation of resonant electromagnetic structure and ionization of gas molecules due to the passage of charged particles.

positive secondaries (+90, +140, +200, and +300 GeV/c) and two momenta with negative secondaries (-90 and -200 GeV/c). The ion chamber calibration obtained from these studies shows about a 6.5% difference over the energy range covered. This change can be understood if the response of the ion chamber is different for protons and pions; the change with energy and beam polarity then just reflects the change in proton and pion fraction in the beam. We believe this difference comes from the difference in the interaction cross section which is ~ 40 mb for pN collisions and ~ 24 mb for πN collisions. A calculation of interactions in the 0.003" Al plates of the ion chamber predicts that ~ 14% additional ion pairs are produced in a proton beam and ~ 8.5% more in a pion beam. This agrees very well with the 6.5% measured difference refered to above and the difference found between the R.F. cavity and the ion chamber. In addition, the results of this calibration agree with the foil irradiation method to better than 2%.

In summary, after taking into account this species dependence of the response of the ion chamber, we succeeded in calibrating the response of the ion chambers with an error of 2.5%.

Particle fractions were measured with a differential Cerenkov counter using He gas as the radiator. The layout of the counter is shown on Figure 7. Cerenkov light with production angles of 0.7 - 1.0 mrad is allowed to pass through the iris and falls onto a photomultiplier's photocathode. The output of the photomultiplier is integrated over the entire beam spill. The pressure of the He in the counter is slowly varied throughout the run; as a result we obtain a response versus pressure that has three distinct peaks due to the three dominant particle species in our beam (π,K and p). The area under each

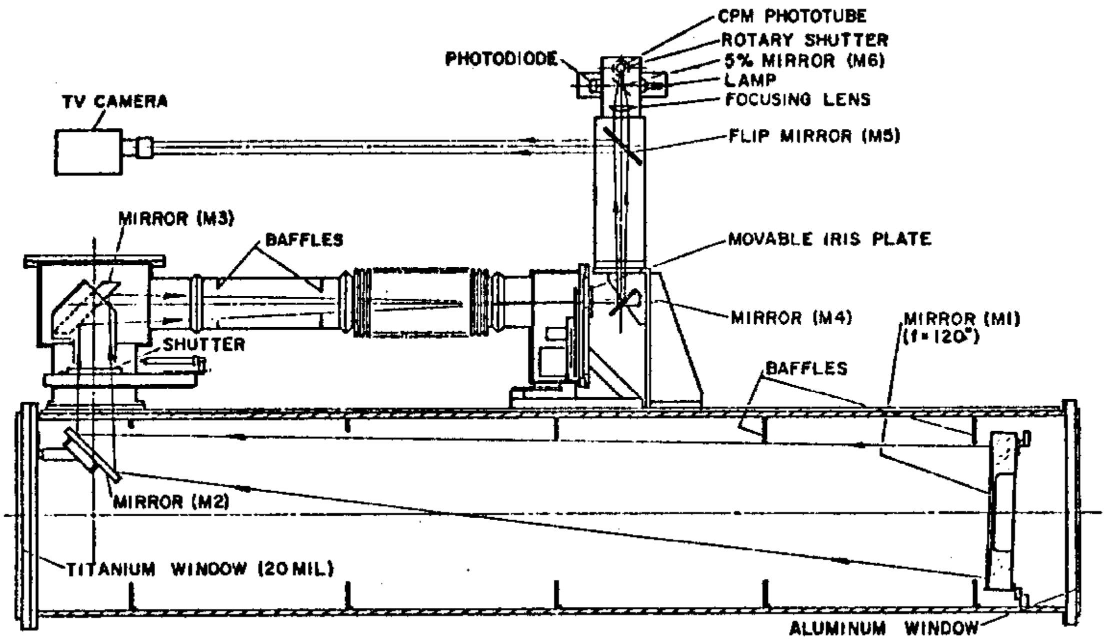

E-616 CERENKOV COUNTER

Fig. 7

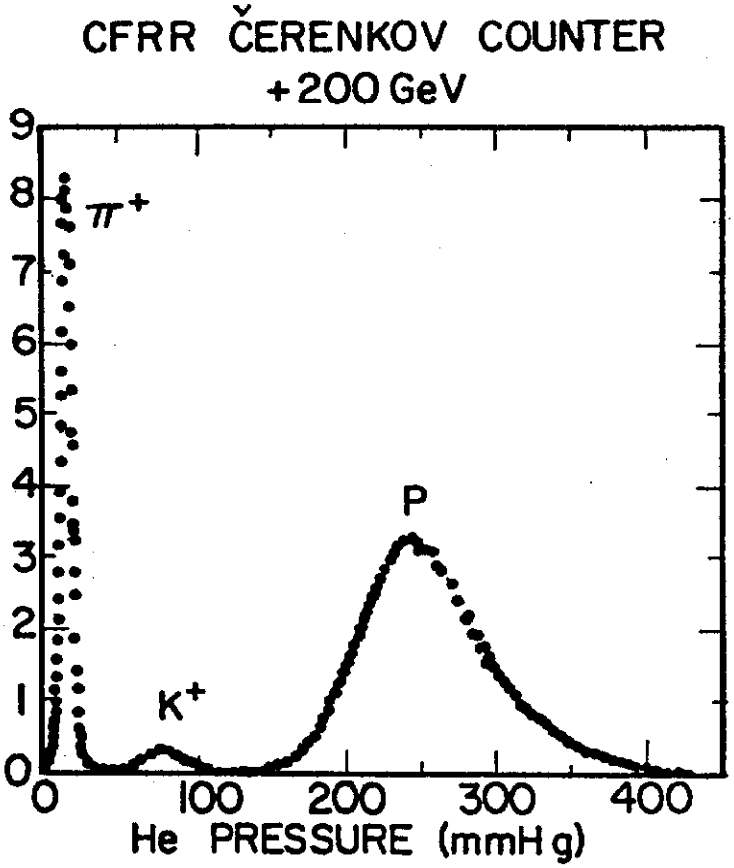

Fig. 8: Cerenkov counter response (normalized to the secondary flux) versus pressure after all corrections and after background subtraction.

peak is a measure of the relative number of particles of that particular particle species.

The number of electrons in the secondary beam was estimated by running the Cerenkov counter in an integrating mode by replacing the annular iris with a 2 mrad hole[6]. The e/π ratio ranged from 6.5% (for 120 GeV/c negative secondaries) to 0.3% (for 250 GeV/c positive secondaries).

The K/π ratio measurements are shown in Fig. 9, and the p/π^+ ratio measurements for positive secondaries in Figure 10. The estimated errors on the particle fractions are 1-3% for pions and 4-7% for kaons. These particle fractions are also in good agreement with recent particle production measurements carried out at CERN[5].

An additional check on these measurements comes from studies of the angular distribution of muons after the beam dump. A segmented ion chamber (the "muon chamber") behind the beam dump (see Fig. 1) measures the number and spatial distribution of decay muons and, therefore, the neutrino flux. This device has not been absolutely calibrated and can only be used to check the relative flux between different momenta and polarities. The pion fluxes obtained with this chamber agree with the above measurements using the Cerenkov counter and ion chamber to better than 1% for negative settings and 7% for positive settings less than 200 GeV/c.

The probability of decay in the decay region is simply derived from a knowledge of the secondary beam mean momentum and the length of the decay pipe. The knowledge of the energy spectrum is crucial, not so much for determining the decay probability, but mostly for inferring the energy and flux of neutrinos at our detector.

From the equation relating the Cerenkov light angle for a particle of mass m and momentum p traveling through a gaseous radiator at pressure P and index of refraction n_o (at 1 atm):

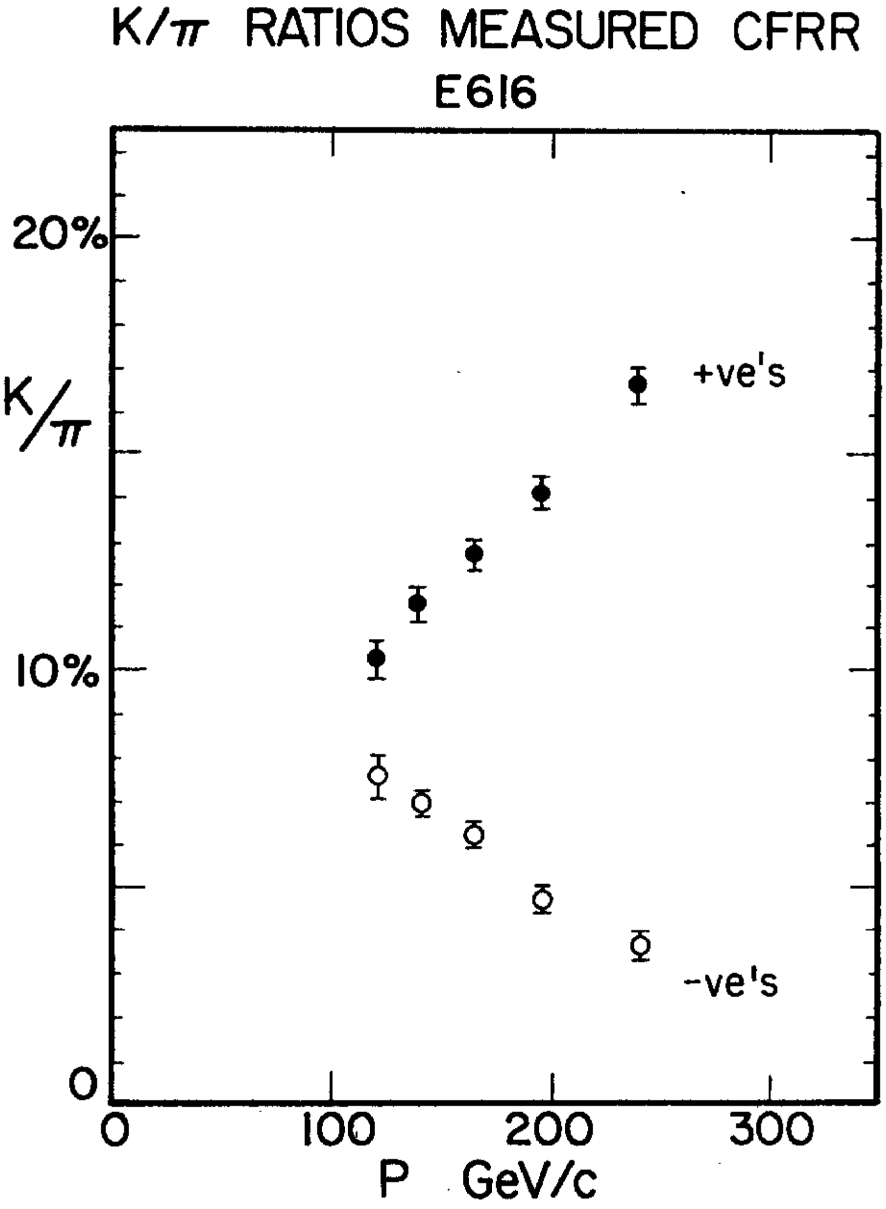

Fig. 9: K/π ratio as a function of the secondary beam momentum.

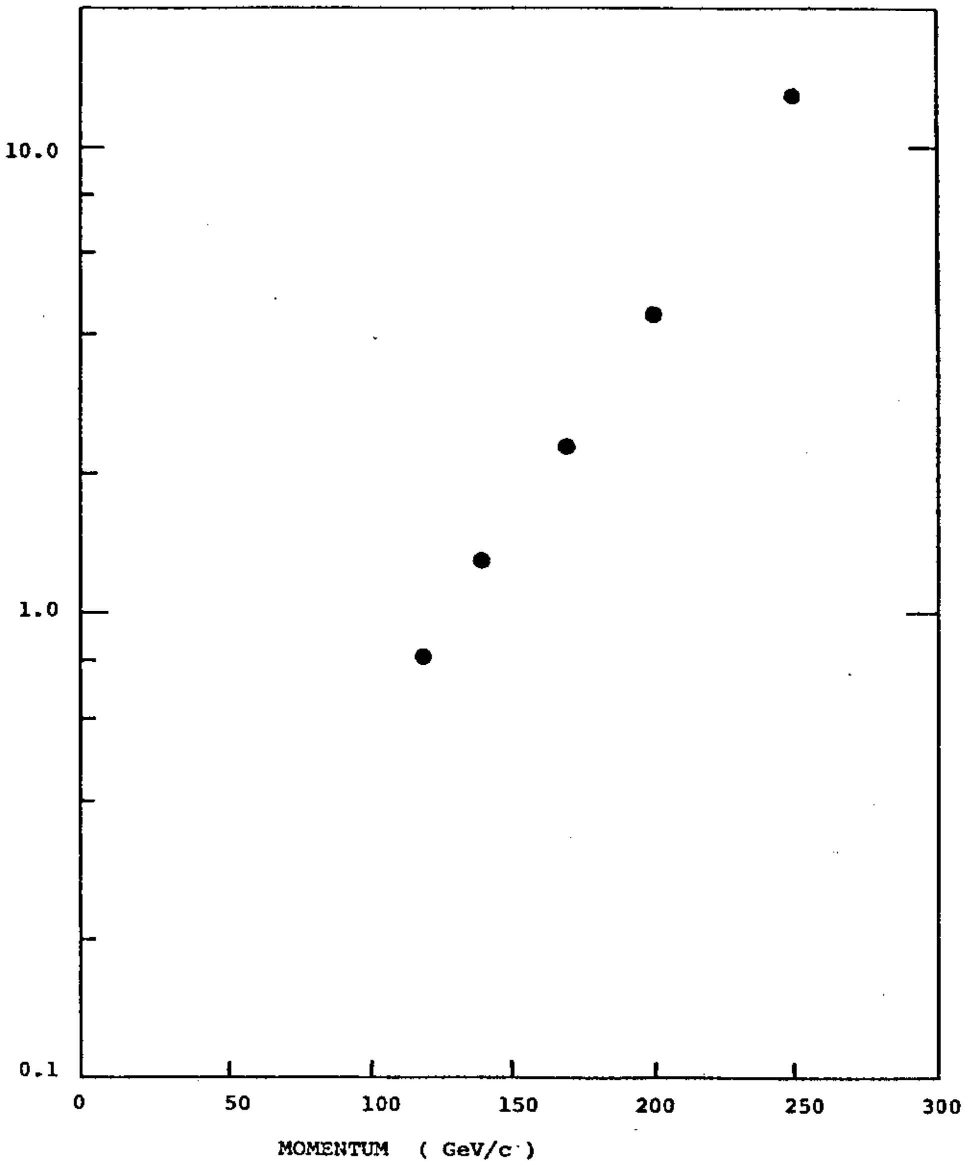

Fig. 10: P/π^+ ratio as a function of the secondary beam momentum.

$$\theta_c^2 = 2(n_o-1)\ P - m^2/p^2$$

(where θ_c is in radians, m in GeV/c^2, p in GeV/c, and P in atm), we see that the location of a peak in our Cerenkov curves is a measure of the particles' mean momentum and that the width of the peak is related to the momentum and angular dispersions of the beam. The index of refraction n_o was measured using monoenergetic 200 GeV/c primary protons. This measurement of n_o to better than 0.1% also maps the counter's response to a monoenergetic beam.

An additional check on this mean momentum is obtained by looking at the total energy of neutrino interactions. As will be discussed in section III, we can select events due to neutrinos from kaon decays for which we have measured the total interaction energy. We thus can obtain a measure of $|P_\nu|=E_\nu=E_{event}$; since the vertex of an event defines the direction of the neutrino, then $\vec{P}_\nu$ is known. We then can calculate the momentum of the parent kaon. This measurement of the K mean momentum is typically accurate at the 2% level. A comparison of the K momentum derived from E_ν measurements in our detector and the K momentum obtained from the Cerenkov study (typical accuracy $\simeq$1%) is shown in Fig. 11. It is seen that the two techniques agree at the 1.5 to 2% level.

The angular divergence of the beam was measured by Segmented Wire Ion Chambers (SWIC) at the two monitoring stations (Fig. 1). These chambers gave us profiles of the beam shape along the horizontal and vertical directions. A small (0.25" x 0.25" x 0.5") movable scintillator located in the first monitoring station (see Fig. 2) was used to cross-check the SWIC profiles. The measured angular divergence was typically .15 mrad in the horizontal direction and .23 mrad in the vertical direction.

Another important function of the SWIC's was to aid in beam steering. Besides monitoring the beam profiles with the SWIC's the signal from steering ionization chamber gaps was used. Each ionization

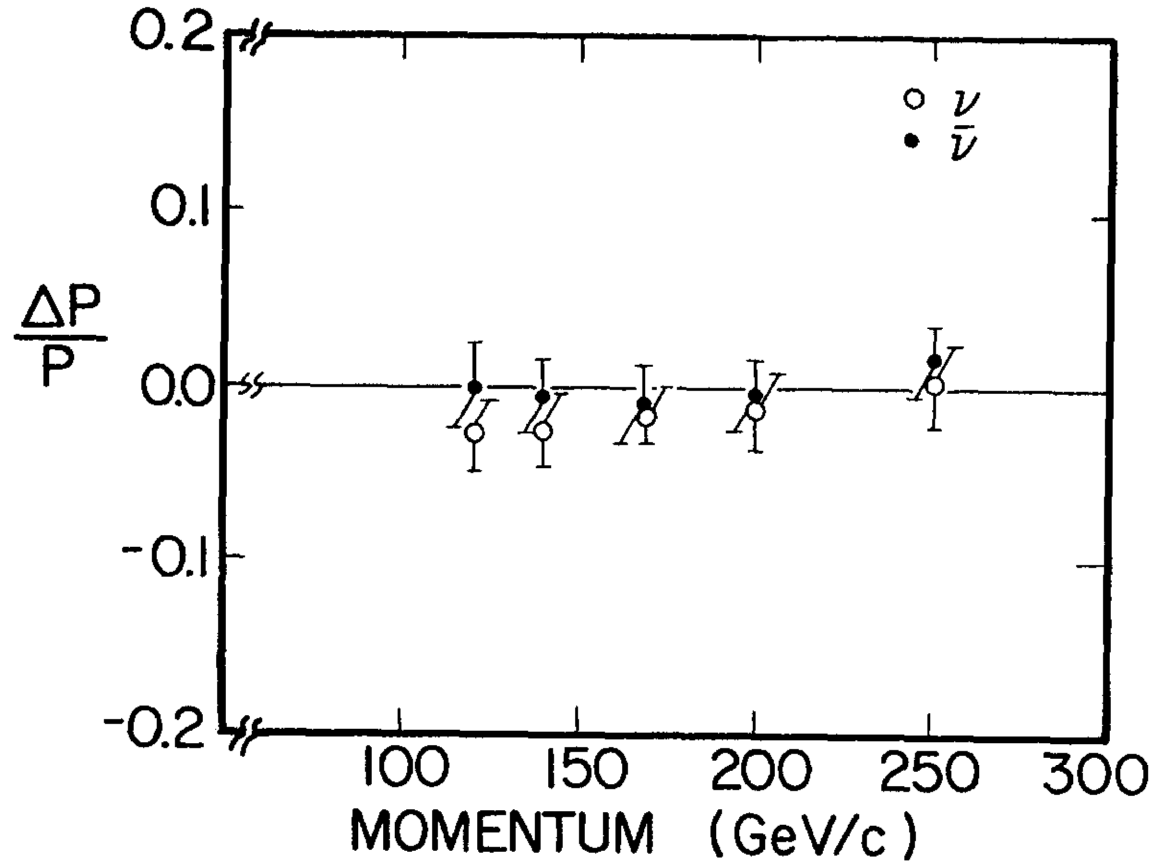

Fig. 11: Fractional difference between the mean kaon momentum as determined from the Cerenkov pressure peaks and the energy of events due to kaon decay neutrinos ($\Delta p \equiv P_{\text{Cerenkov}} - P_{E_\nu}$) versus kaon momentum.

chamber had a pair of split collector plates, one split along the horizontal and one along the vertical. Any mis-steered beam pulses gave different ratios of ions collected in these plates and displaced profiles in the SWIC's. We were able to monitor the beam steering pulse by pulse so as to stabilize the centroid of the neutrino beam at the detector within ± 2.5 cm.

The neutrino flux at our apparatus was determined by a Monte-Carlo simulation which had as an input all of the above measurements. The neutrino energy spectrum with the dichromatic train set to select 200 GeV/c positive secondaries is shown in Fig. 12. The error contributions to the total cross section due to uncertainties of the flux measurement are shown in Table I. We would like to point out that thanks to the high degree of redundancy built into the beam monitoring system we were able to reduce such errors to a level roughly comparable to errors introduced by uncertainties in our apparatus and by event statistics. This should be contrasted to earlier measurements of neutrino total cross sections that are dominated by systematic errors in the determination of the neutrino flux.

III The Neutrino Detector

Our detector, located in Lab E of Fermilab's neutrino area, is shown in Fig. 13. It consists of a calorimeter target followed by an iron toroid muon magnetic spectrometer[6].

The target calorimeter contains 690 tons of square steel plates (10'x10'x2") interspersed with spark chambers (every 20 cm of steel) and liquid scintillation counters[7] (every 10 cm of steel); the target is divided into six independently movable modules. The muon spectrometer consists of three toroidal iron magnets; each toroid has a radius of 5'11" and a central hole (for the excitation coils) of 5" radius.

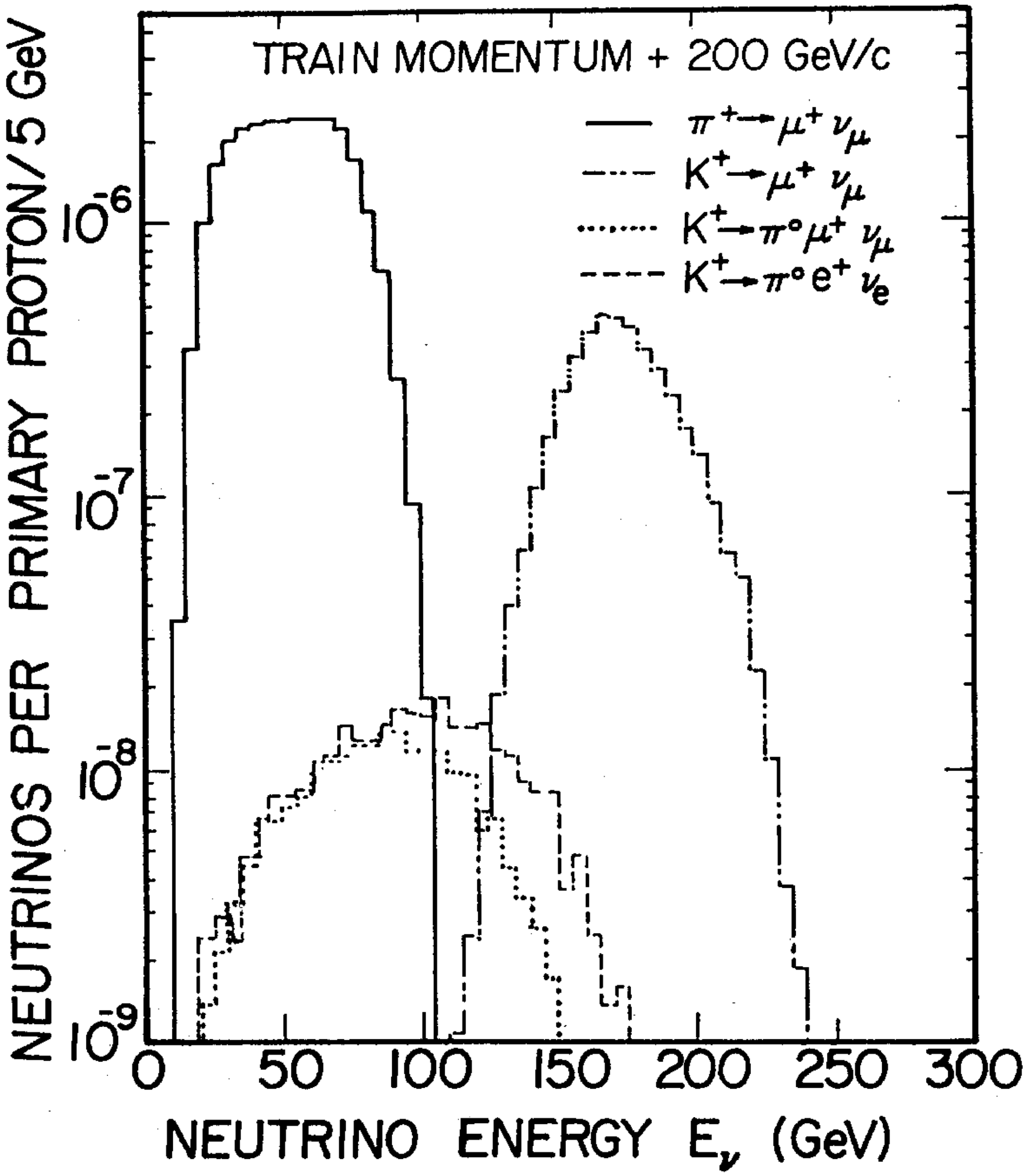

Fig. 12: Energy spectrum for neutrinos within a radius of 50" at our apparatus. The dichromatic train was set to select 200 GeV/c positive secondaries. The contributions due to π decay and various K decay modes are indicated.

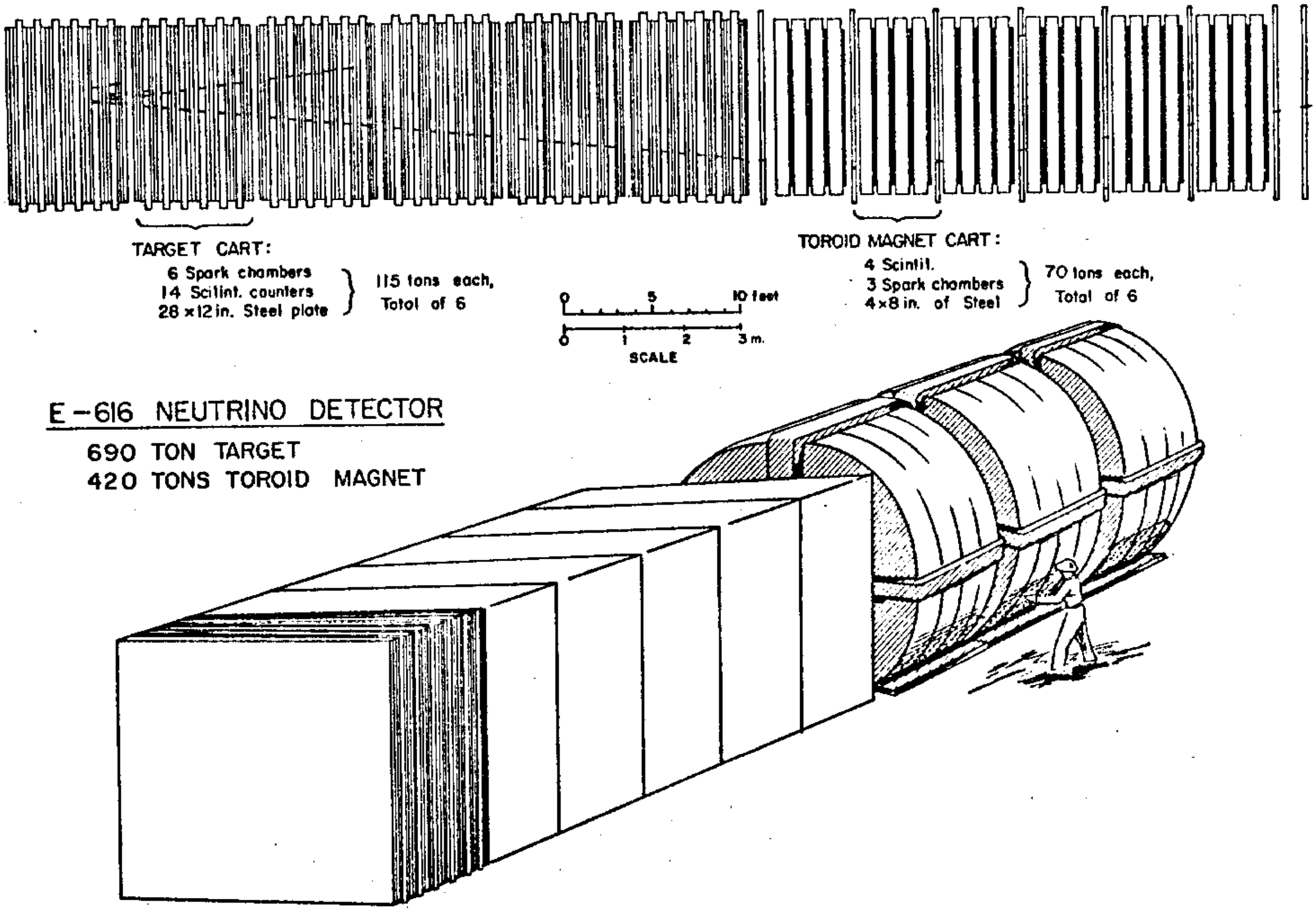

<u>Fig. 13:</u> The Neutrino detector.

Embedded in each toroid there are eight planes of doped acrylic scintillation counters (every 20 cm of steel) and two planes of spark chambers (every 80 cm of steel). Following the spectrometer there are five more planes of spark chambers, the most distant one being 7.5m away from the spectrometer (not shown on Figure 13). The steel made up 94% of the target by weight. The mass, used in calculating the number of target nucleons, was measured during installation and the density agreed with the tabulated value for steel to better than 0.5%.

Hadron energies and muon emission angles are measured in the target calorimeter, and muon momenta are reconstructed in the spectrometer. The target calorimeter modules were calibrated with hadrons transported to Lab E through a hadron beam line running parallel to the earth shield; the spectrometer has been calibrated[8] in the hadron beam line with the line set to transport muons of a known momentum (the results of this study were in good agreement with calculations of $\int B d\ell$). The achieved rms resolutions were:

$$\frac{\Delta P_\mu}{P_\mu} = \sqrt{(.114)^2 + (8.33 \times 10^{-5}\, P_\mu(\mathrm{GeV/c}))^2}$$

$$\Delta\theta_\mu(\mathrm{mrad}) = 0.14 + \frac{57}{P_\mu(\mathrm{GeV/c})}$$

$$\frac{\Delta E_H}{E_H} = \frac{0.89}{\sqrt{E_H(\mathrm{GeV})}}$$

Three types of triggers were used:

1) Muon trigger: A particle was required to penetrate the downstream part of the calorimeter and to reach the middle of the downstream toroid spectrometer. No hadron energy deposition was required. Such events must satisfy the kinematic requirements of $\theta_\mu < 100$ mrad and $P_\mu > 10$

GeV/c. These events allow for full kinematical reconstruction since both the hadron energy and the muon momentum are measured.

2) Penetration trigger: A minimum of 4 GeV of energy must be deposited in the target calorimeter and a particle must penetrate a minimum of 1.6 m of steel. The additional software requirements of $E_H >$ 10 GeV and $\Theta_\mu <$ 370 mrad were imposed. These events include reactions of the type $\nu N \rightarrow \mu^- X$ or $\bar{\nu} N \rightarrow \mu^+ X$ where the muon is produced at large angles, leaves the target calorimeter through its sides, and never reaches the spectrometer. The penetration requirement implies that $P_\mu >$ 2.9 GeV/c.

3) Neutral current trigger: Events in this trigger category must have a minimum of 10 GeV of energy deposited in the target calorimeter, and there must be some signal in two adjacent counters in the target. A software requirement of $E_H >$ 15 GeV was also imposed. The results from the analysis of events satisfying this trigger, i.e. events of the type: $\nu + N \rightarrow \nu + X$ have been reported elsewhere[9]. We will not discuss such results in this paper.

In order to eliminate spurious triggers due to muons originating in the earth shield from neutrino interactions upstream of our detector, the signal from a large scintillator bank (total area 12' x 20') in front of our detector was required in anti-coincidence with all our triggers.

It should be noted that the muon and penetration triggers, which were sensitive to charged current interactions, were to a great extent redundant. These triggers were completely independent in both the counters used and in the logical circuitry used. Typical events lay in a kinematic regime of trigger overlap; about 3/4 of the events satisfied both. Over the kinematic range $\Theta_\mu <$100 mrad and $P_\mu >$ 10 GeV/c the muon trigger was 99.5 ± 0.5 % efficient; over the kinematic range $\Theta_\mu <$ 300 mrad and $E_H >$ 10 GeV the penetration trigger was 100 ± 0.1 % efficient.

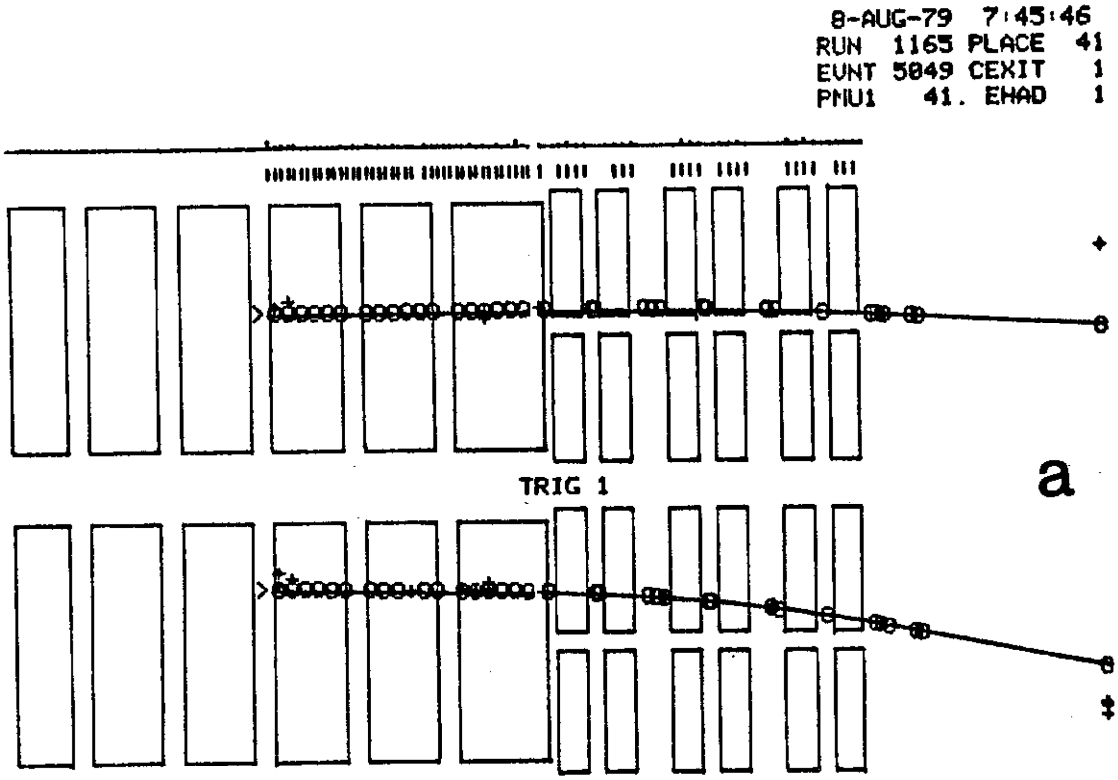
8-AUG-79 7:45:46
RUN 1165 PLACE 41
EVNT 5049 CEXIT 1
PMU1 41. EHAD 1
TRIG 1

a

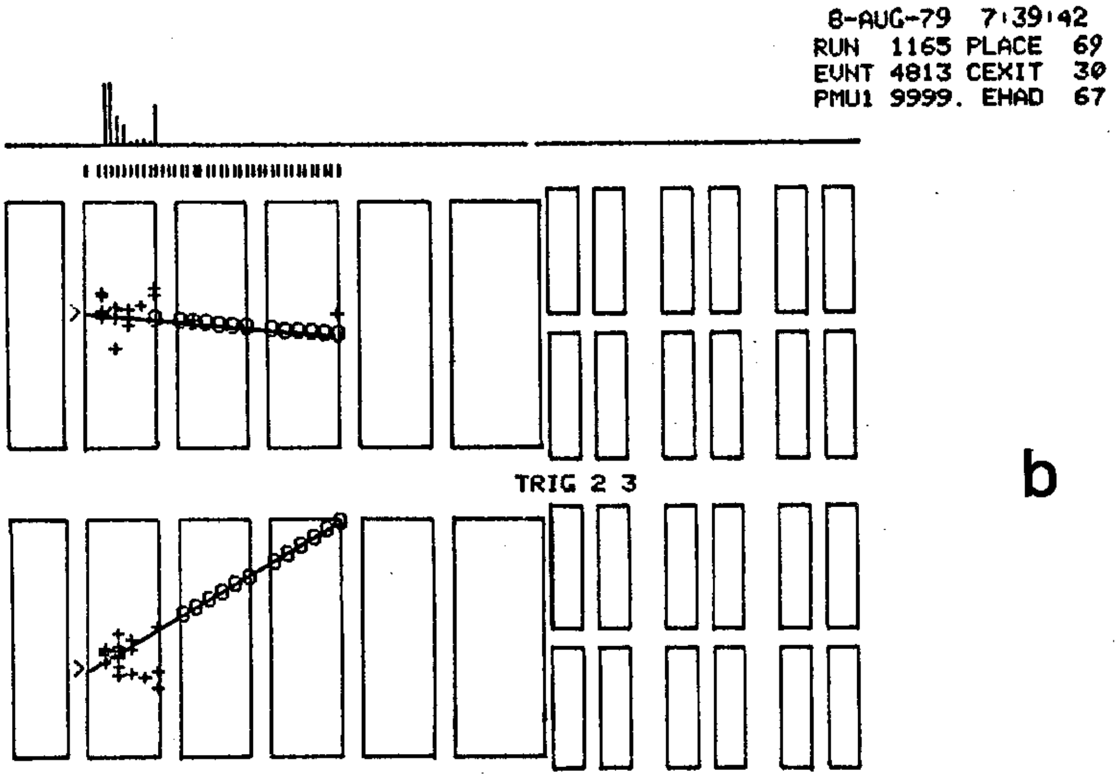
8-AUG-79 7:39:42
RUN 1165 PLACE 69
EVNT 4813 CEXIT 30
PMU1 9999. EHAD 67
TRIG 2 3

b

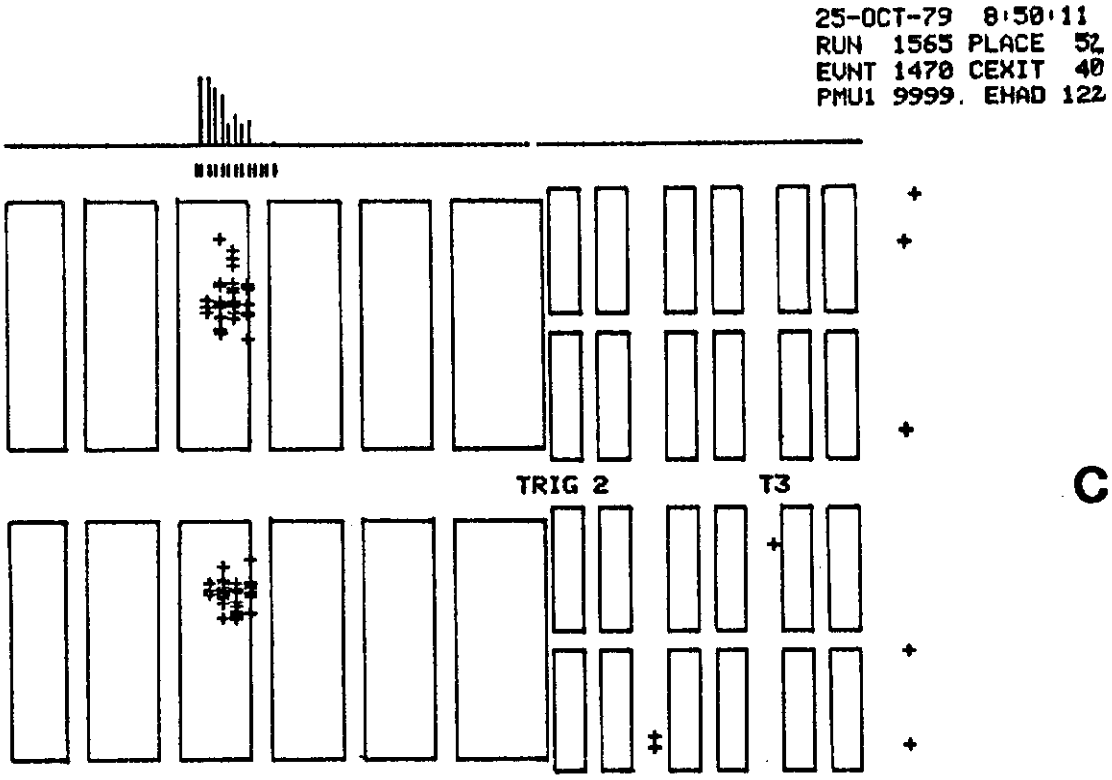

Fig. 14: Computer reconstructed pictures of events. The side (upper half of the figures) and the top view of the apparatus are shown; the small bars above the apparatus indicate scintillator counter latches for counters that fired; the pulse heights in the counters are shown at the very top. Circles signify spark chamber hits associated with a particle track; crosses show spark chamber hits that could not be assigned to a track. These events were obtained with negative secondaries of momentum 250 GeV/c and are due to antineutrino interactions. (a) Muon trigger event, E_H=1 GeV and p_{μ^-} =41 GeV/c. (b) Penetration trigger event, with E_H=67 GeV and Θ_μ =540 mrad. This event, which was later rejected by the software requirement of $\Theta_\mu<370$ mrad, also satisfies the neutral current trigger (i.e. $E_H>10$ GeV). (c) Neutral current trigger, with E_H=122 GeV and no visible muon.

Computer reconstructed event pictures illustrating the three triggers are shown on Fig. 14.

IV Data Analysis and Results

Neutrino and antineutrino data were recorded at five secondary energies (250, 200, 168, 140, and 120 GeV) over a period of eight months ending in January 1980. The total sample included 130,000 charged current neutrino interactions and 23,000 antineutrino interactions. The cross section results shown here correspond to about one-half of the above sample. All events are reconstructed by computer with fiducial and reconstruction cuts applied to limit the sample to regions with good acceptance and small background. With these excessively severe cuts (upstream 75% of the target's length and a radius of interaction less than 50") the fiducial volume is restricted to 286 tons.

Events were binned according to their total measured energy and the radius at which the event occurred in our detector[10]. From the kinematics of the parent pion/kaon decay we expect that for a particular neutrino angle, i.e. for a particular interaction radius, there should be neutrinos of two distinct energies arising from the decay of either pions or kaons. Neutrinos born in kaon decay should have energies near the hadron beam energy and neutrinos from pion decays should cover a range below 0.43 of the beam setting.

For events satisfying the muon trigger the measured energy is $E_\nu = E_H + E_\mu$, that is the total neutrino energy. Fig. 15 is a scatter-plot of the total energy and radius of interaction for such events. The separation into two energy bands is clear. Furthermore, we see that with the chosen secondary beam settings we were able to study neutrino interactions in the energy range E_ν = 30 to 250 GeV.

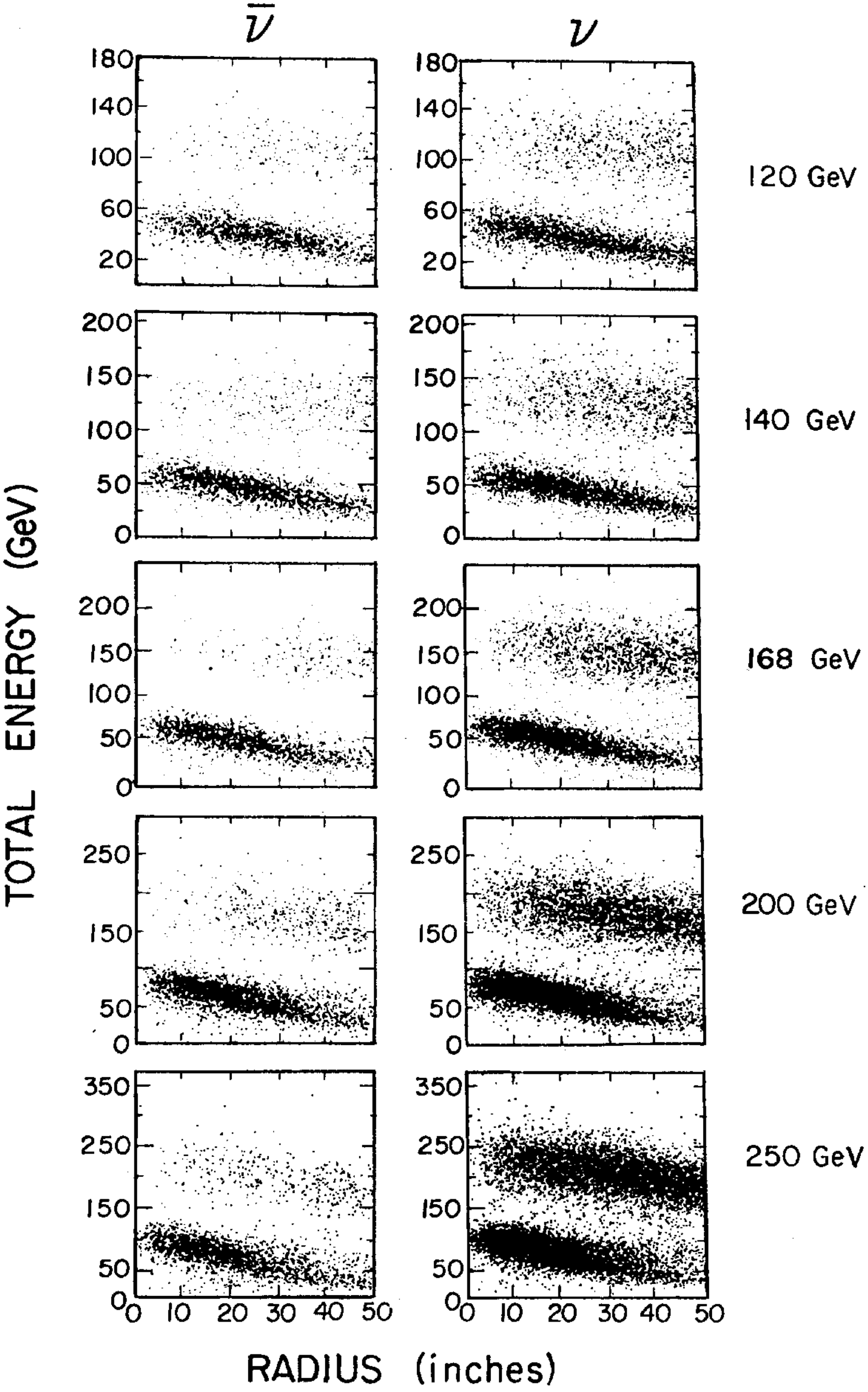

Fig. 15: Plot of the total energy $E_\nu = E_H + E_\mu$ versus the radius of interaction for events satisfying the muon trigger.

In the case of events satisfying the penetration trigger only, i.e. events with a muon for which only the hadronic energy was measured, the neutrino energy is not directly measurable. Nevertheless, such events occur predominantly at high $y = \frac{E_H}{E_\nu}$ values. As illustrated in the acceptance plot of Fig. 16, a substantial fraction of the kaon neutrino events of this type have a hadronic energy which is larger than E_π, the maximum hadronic energy possible for a pion neutrino interaction. Therefore such events were unambiguously identified as due to kaon neutrino interactions. If the hadronic energy is lower than E_π and greater than 10 GeV the muon trigger has very high acceptance for events due to kaon neutrinos. The small fraction of kaon neutrino events not satisfying the muon trigger was determined from the kaon neutrino events satsfying the muon trigger by a geometrical correction. The remaining events in this hadronic energy band are then due to pion neutrinos. Finally, for events with hadron energy less than 10 GeV the muon trigger acceptance is 100%, since the muon production angle is constrained by kinematics to be very small. For these events the total neutrino energy is measured and they can always be identified as pion or kaon neutrino interactions. We have considered the possibility for crossover of events due to misidentification; the contribution to the errors in the total cross section due to this proccess is also shown in Table I.

Corrections were made for neutrinos arising from decays upstream of the decay region (5%) and cosmic ray contamination (0.5%). These were measured directly by recording data at times when the beam entering the decay region was blocked, and in the 10 s intervals between the 2ms beam bursts, respectively. Calculated rates were used to correct for the contribution from three body decays of kaons (1-2%).

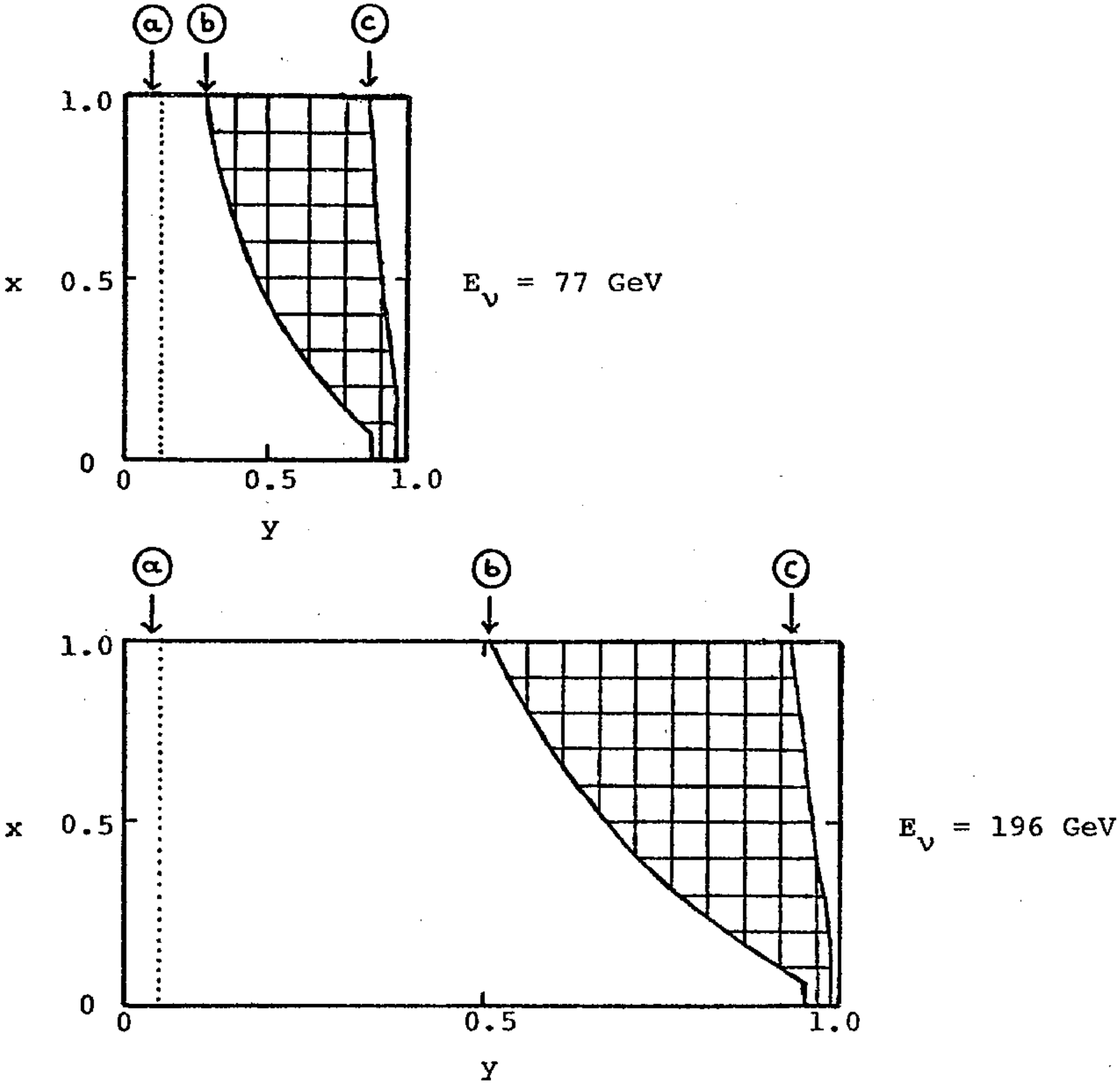

Fig. 16: Acceptance regions in the $x = \frac{Q^2}{2M_N E_H}$ and $y=E_H/E_\nu$ plane, for events with neutrino energies of 77 and 196 GeV. These neutrino energies correspond to the average neutrino energy for events with interaction radius of 5" to 10" and for a secondary beam momentum of 200 GeV/c. The muon trigger events accepted lie to the left of the line marked (b), which indicates the $\Theta_\mu<0.1$ and $P_\mu>10$ GeV/c cuts. Events that satisfy the penetration trigger lie between the lines marked (a) and (c). Line (a) reflects the $E_H>10$ GeV cut and line (c) the $\Theta_\mu<0.37$ and $P_\mu>2.9$ GeV/c cuts. Events satisfying the penetration trigger only lie in the cross-hatched region. The horizontal scale of the acceptance plots has been made proportional to the neutrino energy to facilitate energy comparisons. Geometrical inefficiencies due to the finite size of our apparatus are not included.

Further corrections were made for geometrical inefficiency, and the unsampled region at high $x = \frac{Q^2}{2M_N E_H}$ and high y. Geometrical inefficiency is corrected by a model independent method in which observed events are weighted by an efficiency factor. The efficiency factor is calculated by rotating the observed event around the beam direction, translating it along the beam direction, and determining if the event would be accepted with the new vertex and orientation. The correction for the unsampled kinematical region was based on a simple extrapolation using Buras - Gaemers type parametrizations of published nucleon structure functions[11]. This correction was typically of the order of 2%, and it was large (8%) only for neutrino events at low energy. The same parametrization was used to convert our results from cross-section/nucleon on an iron target to cross-section/nucleon on a pure isoscalar target (+ 1.4% for antineutrinos, -2.1% for neutrinos).

Finally we correct for apparatus deadtime effects due to the inability of the apparatus to respond while recording data. They were measured in two ways: by recording the flux transmitted during the live and dead times, and by counting the triggers during the two times. The two methods agreed to 1.2%.

With the events corrected and separated according to their interaction radius and neutrino type, total cross sections for each beam setting were formed using the neutrino energy and flux distributions described previously. Table I gives the typical errors from the most relevant uncertainties in determining the cross sections.

Fig. 17 shows the neutrino and antineutrino cross sections divided by energy for the combined data; the measurements[12] by the CDHS collaboration are also shown for comparison. (Checks made in regions where different settings overlap show the cross sections to agree within statistical errors.) The average total cross section slopes for the range 40-200 GeV are:

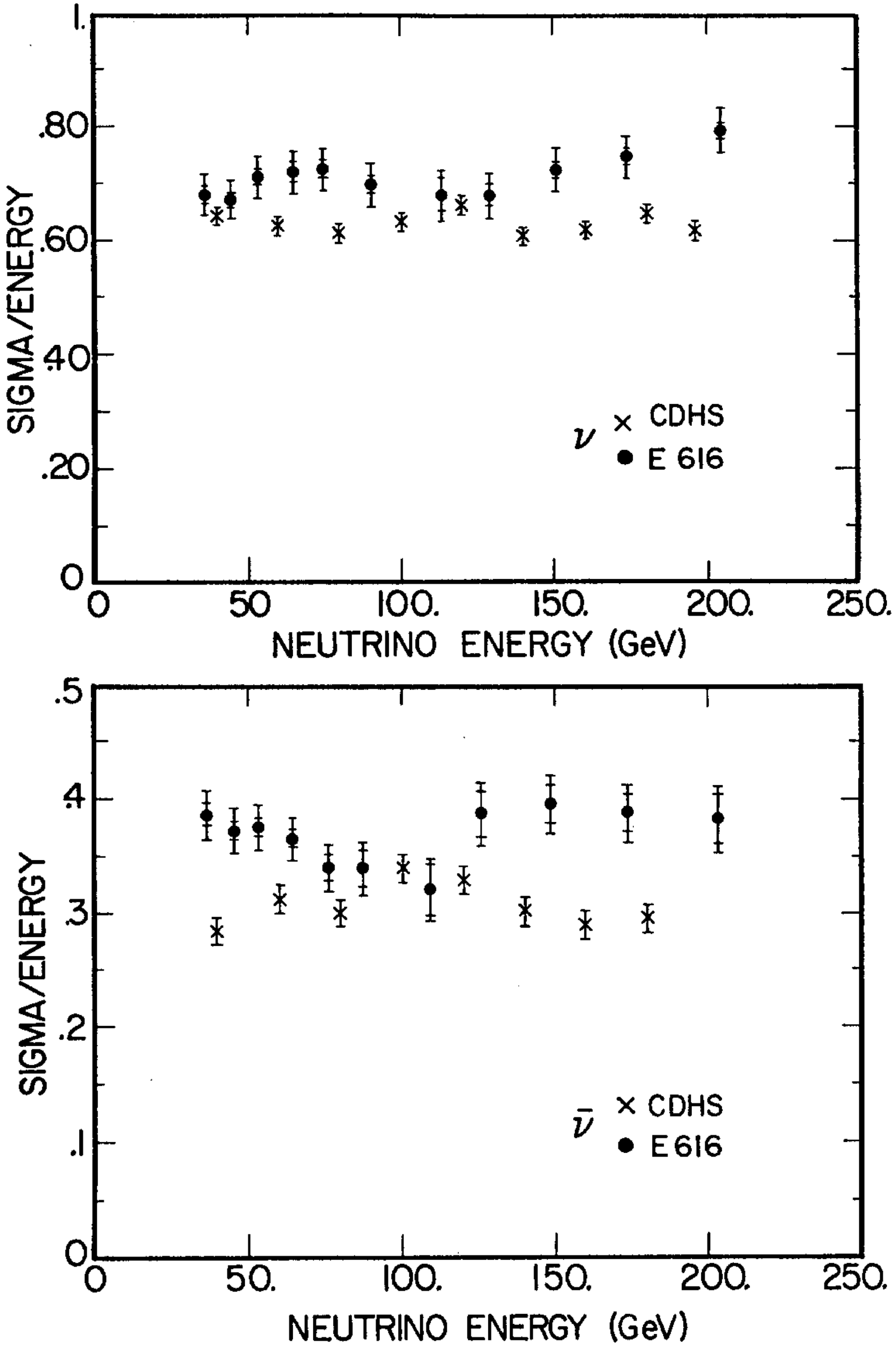

Fig. 17: Ratio of total cross section to energy versus energy for incident neutrinos and antineutrinos. The inner bars for the E616 data (this experiment) are statistical errors only; outer error bars include systematic errors. The CDHS data are from Ref. 12, the error bars are statistical errors only. $\frac{\sigma}{E}$ is given in units of 10^{-38} cm^2/GeV.

$$\frac{\sigma_\nu}{E_\nu} = 0.720 \pm 0.0037 \pm 0.0138 \pm 0.026 \times 10^{-38} \text{ cm}^2/\text{GeV}$$

$$\frac{\sigma_{\bar\nu}}{E_{\bar\nu}} = 0.360 \pm 0.0035 \pm 0.0086 \pm 0.0211 \times 10^{-38} \text{ cm}^2/\text{GeV}$$

where the first error is statistical, the second is due to systematic point-to-point variations, and the third is an overall systematic error in the normalization. The data shows no striking energy dependence and are consistent with a σ_ν/E_ν which is constant with energy [13]. These values are somewhat higher than previously published values, as illustrated in Table II. Many of the participants in this measurement also participated in the earliest measurement (entry 1). The beam, the flux monitoring equipment, the calibration techniques, and the neutrino detector have been completely rebuilt and are considerably more sophisticated than the earlier apparatus. It should also be noted that the calibration technique used in this experiment for obtaining neutrino flux is different than that used in entries (2) and (3).

From the differential form of the neutrino-nucleon cross-section,

$$\frac{d^2\sigma^{\nu(\bar\nu)}}{dxdy} = \frac{G^2 M_N E_\nu}{\pi}\left[(1-y)\, F_2(x,Q^2) + xy^2\, F_1(x,Q^2) \pm (y-y^2/2)\, xF_3(x,Q^2)\right]$$

the ratio,

$$R = \frac{\sigma_L}{\sigma_T} = \frac{F_2 - 2xF_1}{2xF_1} + \frac{2M_N^2 x^2 F_2}{Q^2 x F_1} \approx \frac{F_2 - 2xF_1}{2xF_1}$$

the quark-parton relations,

$$2\,x\,F_1 = q(x) + \bar{q}(x) = u(x) + d(x) + s(x) + c(x) + \bar{u}(x) + \bar{d}(x) + \bar{s}(x) + \bar{c}(x)$$

$$x\,F_3^{\nu} = q(x) - \bar{q}(x) + 2\,\bar{s}(x) - 2\,\bar{c}(x)$$

and assuming approximate scaling (i.e. $F_{1,2,3}(x,Q^2) = F_{1,2,3}(x)$) we obtain:

$$\sigma^{\nu(\bar{\nu})} = \frac{G^2 M_N E_\nu}{\pi}\left(\frac{4+3R}{6(1+R)} f_2 \pm \frac{1}{3} f_3\right)$$

We have set $f_1 = \int xF_1\,dx$, $f_2 = \int F_2\,dx$, and $f_3 = \int xF_3\,dx$. Neglecting the contribution of the strange and charmed sea to f_3 we have:

$$f_3 = \frac{3\pi}{2G^2 M_N E_\nu}(\sigma^{\nu} - \sigma^{\bar{\nu}})$$

$$f_2 = \frac{3\pi}{G^2 M_N E_\nu}(\sigma^{\nu} + \sigma^{\bar{\nu}})\,\frac{1+R}{4+3R}$$

$$Q + \bar{Q} = \int (q(x) + \bar{q}(x))dx = 2\,f_1$$

$$Q - \bar{Q} = f_3$$

Table II also shows these integrated structure functions and the quark/antiquark momentum fractions ($Q/\bar{Q}$) for the nucleon, assuming that $R = 0.1$. This measurement implies that the momentum carried by interacting constituents, i.e. the quarks, as measured by neutrinos, is more than 50% of the total nucleon momentum. This contrasts with previous measurements in which a smaller momentum fraction was found.

The differential distribution $d\sigma/dy$ can be used as a consistency check. We should have:

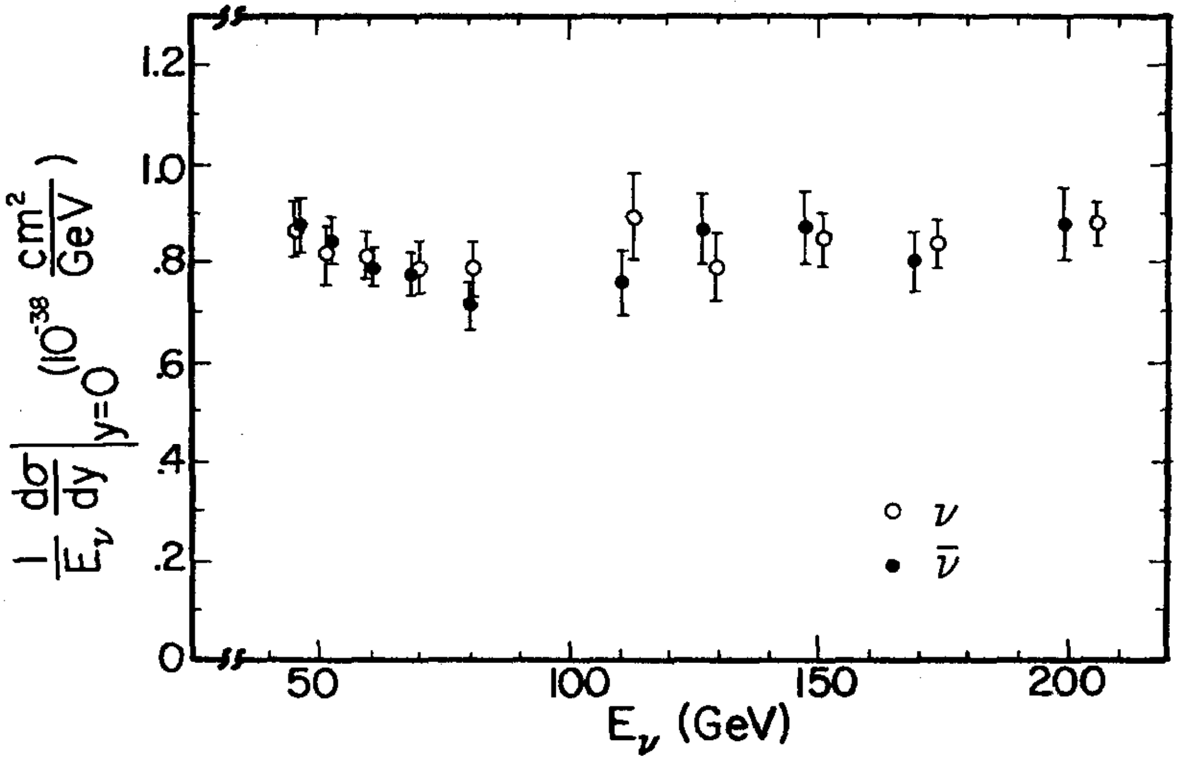

Fig. 18: $\frac{1}{E}\ \frac{d\sigma}{dy}\Big|_{y=0}$ versus energy for incident neutrinos and antineutrinos on an isoscalar target. Radiative corrections[15] (for radiative processes in the final state) have been applied.

$$\frac{1}{E_\nu}\frac{d\sigma^\nu}{dy}\bigg|_{y=o} = \frac{1}{E_{\bar\nu}}\frac{d\sigma^{\bar\nu}}{dy}\bigg|_{y=o} = \frac{G^2M_N}{\pi}(Q + \bar{Q})(1 + R)$$

Fig. 18 shows a plot of this quantity as a function of the neutrino's energy. It can be seen that the neutrino and antineutrino data at each energy are consistent with this equality.

A more detailed study of the differential cross section $\frac{d\sigma^2}{dxdy}$ is currently under way. This study will culminate with the extraction of structure functions. We expect that since the structure function normalization is directly related to the total cross section, the structure functions extracted by our experiment should be larger than those measured previously. Fig. 19 shows our preliminary results for $F_2(x)$ compared to the CDHS structure functions[16] for the Q^2 bin 4 to 8 GeV^2/c^2.

As expected our results are higher than those of CDHS especially in the low x region. (The analysis for both CDHS and this experiment assumes R = 0.1, where the exact form of R was used, and corrects for neutron excess in iron, strange sea quarks with $2s/(\bar{u}+\bar{d}) = 0.35$, and radiative corrections[15].) Also shown are data from the SLAC eD experiment[17] using the 5/18 rule to allow the comparison of neutrino and electron scattering. The SLAC data agree well with our data but are somewhat higher than CDHS.

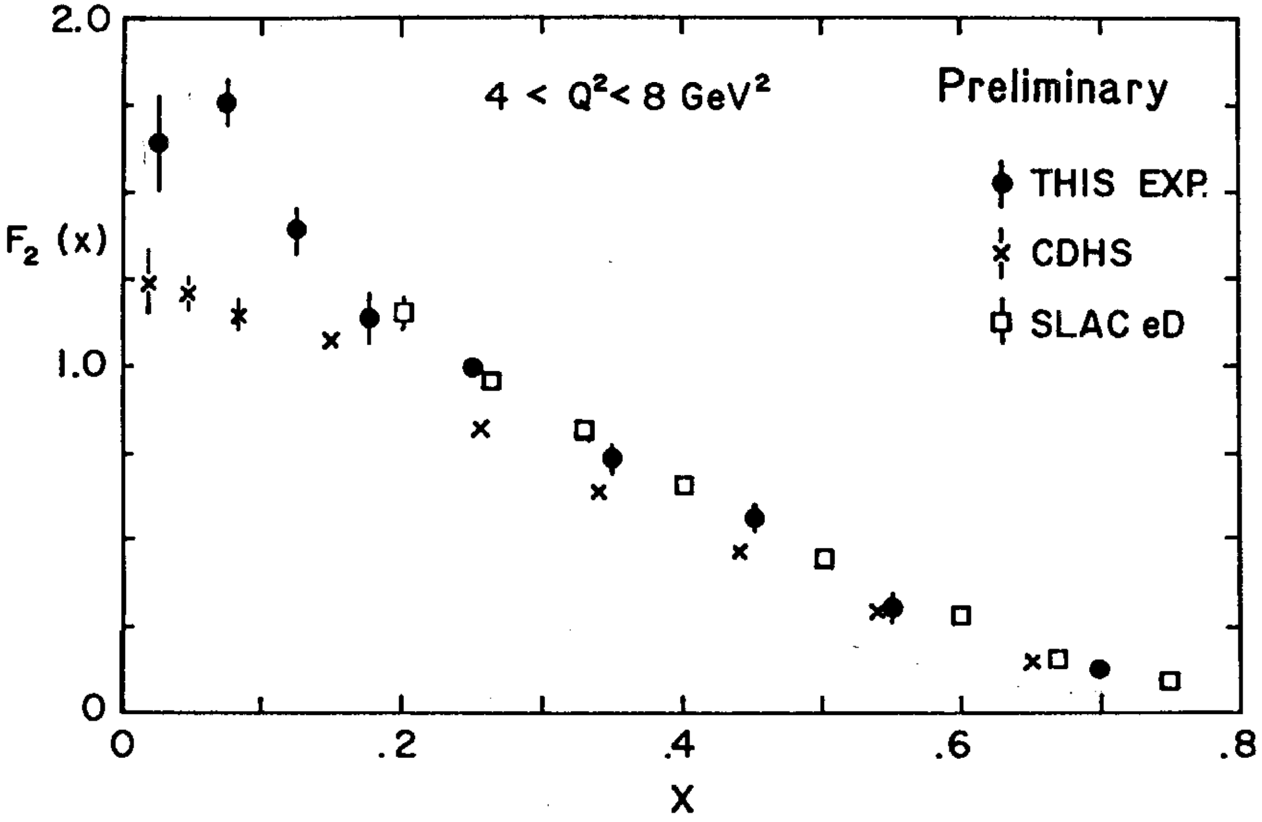

Fig. 19: $F_2(x)$ for the Q^2 bin 4 to 8 GeV^2/c^2. Errors are statistical only. The CDHS data are from Ref. 16. The SLAC eD data are from Ref. 17; the SLAC eD data have been multiplied by 18/5.

Table I:

Approximate errors in cross sections and their sources. Actual errors depend on energy setting and position in target.

		ν_π	ν_K
1.	Statistical counting errors, including empirically subtracted backgrounds.	3%	8%
2.	Particle fractions (π/K/P).	(1-4)%	(4-7)%
3.	Monitoring stability and calibration.	(2-5)%	(2-5)%
4.	Crossover of events $\nu_\pi \leftrightarrow \nu_K$.	0.7%	2.5%
5.	Neutrino angle error.	3%	2%
6.	Neutrino energy error.	1.5%	1.5%
7.	Deadtime uncertainty.	1%	1%

Table II

Values of ν_μ and $\bar{\nu}_\mu$ cross section slopes and structure function integrals in the range $40 < E_\nu < 300$ GeV for an isoscalar target.

Expt.	$(\sigma/E)^{\nu}$ †	$(\sigma/E)^{\bar{\nu}}$ †	$f_2=\int F_2 dx$ *	$f_3=\int xF_3 dx$	Q *	$\bar{Q}$ *
1. CITFR[10]	0.609±0.03	0.290±0.015	0.447±0.017	0.309±0.033	0.358±0.022	0.049±0.013
2. BEBC[14]	0.630±0.05	0.290±0.03	0.457±0.029	0.330±0.056	0.373±0.036	0.043±0.025
3. CDHS[12]	0.620±0.05	0.300±0.02	0.457±0.027	0.310±0.052	0.363±0.036	0.053±0.019
4. This Expt.	0.720±0.030	0.360±0.023	0.524±0.018	0.341±0.036	0.409±0.022	0.067±0.018

* The values of $\int F_2 dx$, Q, and $\bar{Q}$ depend on the assumed value of $R = \sigma_L/\sigma_T$. The value $R = 0.1$ has been assumed. The change in these integrals is typically about ±0.012 for $\Delta R = \pm 0.1$.

† σ/E is given in units of 10^{-38} cm^2/GeV.

References:

1. For a recent review of lepton-nucleon scattering see: F. Sciulli in *Proceedings of the 20th International Conference of High Energy Physics*, Madison, Wisconsin, July 17-23, 1980, edited by L. Durand and L.G. Pondrom, p. 1279.

2. D.A. Edwards, S. Mori, and S. Pruss, Fermilab TM-661, 1976 (unpublished).

3. A.R. Donaldson, IEEE Transactions on Nuclear Science, *NS-26*, 3439 (1979).

4. A. Chapman-Hatchett *et al.*, SPS/ABT/INT. 79-1, 1979 (unpublished).

5. H.W. Atherton *et al.*, CERN 80-07, 1980 (unpublished)

6. For a detailed description consult J.R. Lee, Thesis, California Institute of Technology, 1980 (unpublished).

7. B.C. Barish *et al.*, IEEE Transactions on Nuclear Science, *NS-25*, 532 (1978).

8. A. Bodek *et al.*, University of Rochester preprint UR-804,(to be published).

9. R. Blair *et al.* in *Neutrino-81, Proceedings of the International Conference on Neutrino Physics and Astrophysics*, Wailea, Hawaii, July 1-8, 1981, talk presented by M. Shaevitz (to be published).

10. Our procedure is essentially the same as the one described in: B.C. Barish *et al.*, Phys. Rev. Lett. *39*, 1595 (1977); B.C. Barish *et al.* in *Proceedings of the Third International Conference on New Results in High Energy Physics*, Vanderbilt University, Nashville, Tennessee (1978).

11. A. Para in *Proceedings of the 1979 International Symposium on Lepton and Photon Interactions at High Energy*, Fermilab, August 23-29, 1979, edited by T.B.W. Kirk and H.S.I. Abarbanel, p. 343.

12. J.G.H. de Groot *et al.*, Z. Phys. *C1*, 143 (1979).

13. It should be noted that our data give a marginally better fit to a conventional two neutrino oscillation model with $\Delta m^2=350 eV^2/c^2$, $\sin^2 2\alpha=.18$, but such a fit is *not* required by the data. On the other hand there are no independent data that can exclude such a possibility. We are currently installing a second smaller detector to investigate this exciting possibility.

14. P.C. Bosetti *et al.*, Phys. Let. *70B*, 273 (1977).

15. A. De Rujula, R. Petronzio, and A. Savoy-Navaro, Nucl. Phys. *B154*, 394 (1979).

16. F. Eisele in *Neutrino-81, Proceedings of the International Conference on Neutrino Physics and Astrophysics*, Wailea, Hawaii, July 1-8, 1981 (to be published).

17. A. Bodek *et al.*, Phys. Rev. *D20*, 1471 (1979).